scientific reports

Check for updates

OPEN

Electrostatic enhanced terahertz metamaterial biosensing via gold nanoparticles integrated with biomolecules

Min Zhang[1], Liwen Jiang[2], Shuo Wang[3], Shoujun Zhang[2], Meng Liu[1], Yuping Zhang[1], Huiyun Zhang[1]✉ & Zhen Tian[2,3]✉

Terahertz spectroscopy has drawn great interest for the detection and characterization of biological matter, but its limited sensitivity to biomolecules with weak changes in dielectric properties with varying concentration has hinders potential bio-sensing applications. Here, a novel terahertz sensor was developed for enhancing the ability to detect biomolecules based on two electromagnetically induced transparency (EIT) metamaterials coupled with gold nanoparticles (AuNPs) integrated with biomolecules. The electrostatic interaction between AuNPs and positively charged biomolecules generates localized field enhancement at the biomolecule–metamaterial interface, resulting in a threefold increase in sensitivity for positively charged histidine that exhibit weak dielectric property changes with varying concentration. As a contrast, glucose shows a weaker effect due to its electrostatically neutral nature. Experimental studies reveal that by evaluating the modulation depth (MD) and modulation enhancement (ME) factors of the transmission peak for histidine and glucose in the presence of AuNPs, we achieve and enhance intuitive detection and discrimination of these biomolecules. Additionally, a two-EIT metamaterial with a 1 × 2 pixel array enables multiparameter imaging, visualizing the concentration and spatial distribution of biomolecules. Our results not only significantly improve the response sensitivity of biomolecules with weak dielectric properties in the terahertz domain, but also provide a new idea for developing high-sensitivity functionalized terahertz biosensors and advancing multi-biomolecular analysis and imaging techniques.

Keywords Terahertz metamaterial, Gold nanoparticles, Electrostatic-enhanced, Biomolecules detection

Terahertz spectroscopy, recognized for its low energy, high transmissivity, and sensitivity to the vibrational modes of specific biomolecules, demonstrates high potential for applications in biomedical detection and sensing[1–3]. Although certain biomolecules exhibit characteristic frequencies within the terahertz range, their small molecular size often limits effective interaction with terahertz waves, posing significant challenges for achieving high-sensitivity detection and precise differentiation of target biomolecules[3–6]. Traditional terahertz spectroscopic methods were typically average response intensities, which obscure subtle variations among distinct biological targets[7,8]. Recent studies have demonstrated that leveraging metamaterials to enhance the interaction between terahertz waves and small biomolecules can elevate the biological detection capabilities of terahertz spectroscopy[9–11]. Terahertz metamaterials, composed of periodic subwavelength unit arrays, are engineered structures that leverage unique electromagnetic properties[12–15]. Owing to their remarkable advantages, considerable research has been directed toward exploring their multifunctionality and exceptional effects, including circular dichroism, EIT, and near-perfect absorption[16–19]. Notably, THz metamaterials featuring EIT windows have shown relatively high sensitivity in biosensing and biomolecular detection, driven by resonance coupling strength and shifts in resonance frequency[20–22]. Furthermore, EIT terahertz metamaterials with multiple resonance-coupling bands hold immense potential for distinguishing a diverse range of biomolecules, such as amino acids, sugars, etc[23,24]. Despite their remarkable advantages, most available

[1]College of Electronics and Information Engineering, Shandong University of Science and Technology, Qingdao 266510, China. [2]Center for Terahertz Waves and Key Laboratory of Optoelectronics Information and Technology (Ministry of Education), Tianjin University, Tianjin 300072, China. [3]School of Precision Instrument and Optoelectronics Engineering, Tianjin University, Tianjin 300072, China. ✉email: sdust_thz@126.com; tianzhen@tju.edu.cn

terahertz metamaterial sensors continue to face challenges, including limited detection sensitivity and accuracy when applied to biomolecules[25–27]. For instance, biomolecules that undergo polarization saturation at low concentrations exhibit minimal changes in dielectric properties, thereby limiting the ability of metamaterial sensors to enhance their response sensitivity[28–31]. Recent advancements have led to the development of nanoscale integrated architectures based on optical and electronic systems, enhancing the sensitivity of biomolecular detection, such as plasmonic biosensors utilizing nanoparticles[32,33]. However, these systems still fall short of meeting the increasing demand for on-chip, label-free, selective, reproducible, low-cost, ready-to-use, and ultra-sensitive biosensors. Moreover, the lack of plasmonic activity of AuNPs in the terahertz frequency range significantly limits their applicability in this domain[34]. Some pioneering studies have demonstrated that combining terahertz metamaterials with nanoparticles results in further boosting of performance specifications[34]. AuNPs exhibit excellent biocompatibility and versatile surface functionalization capabilities, allowing them to bind with various functional groups, such as carboxyl, amine, and thiol groups[35,36]. In particular, carboxyl-modified AuNPs carry a negative charge and can form strong electrostatic bonds with the positively charged groups of biomolecules, while preserving the biological properties of the molecules[37,38]. These functionalized metallic nanoparticles are exploited to optimize the binding strength between the biomolecules and resonant-coupling unit cells[34,39]. Histidine, as a naturally occurring essential amino acid, has attracted particular attention because it carries positive charges under acidic and near-neutral pH conditions, enabling strong electrostatic interactions with negatively charged carboxyl-modified AuNPs[40,41]. Moreover, histidine plays essential roles in protein structure, enzymatic catalysis, and broader biological processes, making its non-destructive detection highly significant for biomedical research[42–44]. Previous studies have demonstrated that histidine exhibits characteristic absorption peaks in the range of 0.8 THz to 2.5 THz, indicating its unique vibrational modes within this frequency domain[45]. Recent investigations have explored the detection and molecular vibrational modes of histidine in terahertz frequencies[46]. However, owing to the inherently weak dielectric response of histidine, traditional terahertz detection methods encounter significant challenges in enhancing sensitivity[45]. AuNPs, as novel sensitivity improvement tools, have notable potential in the detection of histidine biomolecules. However, the mechanisms of enhanced terahertz metamaterial response have not been fully elucidated. Thus, a systematic investigation is required to explore the effects of integrating AuNPs with positively charged histidine solutions and electrically neutral biomolecule solutions (e.g., neutral glucose) on the sensitivity of terahertz metamaterial sensors, respectively. Furthermore, the feasibility of aligning the characteristic frequencies of biomolecules with the resonance-coupling frequencies of metamaterials to further improve sensor selectivity and sensitivity remains unverified.

In this study, we developed a terahertz biosensor based on two-EIT metamaterials coupled with AuNPs integrated with biomolecules, to enhance the label-free detection and distinguish capabilities of various biomolecules. We first designed a two-EIT terahertz metamaterial structure with multiple resonance-coupling bands, formed by periodic unit cells that combine resonant elements exhibiting both inductor-capacitor (LC) resonance mode and dipole resonance mode. The resonance coupling between the LC resonance mode and dipole resonance mode resonators enabled the emergence of three resonant frequency bands and two EIT transparency peaks in the terahertz metamaterial. Using this two-EIT metamaterial as a biosensing platform, solutions of positively charged histidine and electrostatically neutral glucose were crystallized, both with and without AuNPs, onto the surface of the metamaterial. We systematically examined the impact of integrating carboxyl-modified AuNPs with histidine and glucose solutions of differing charge characteristics on the terahertz metamaterial's response sensitivity. Additionally, we investigated the effect of terahertz metamaterials on the sensitivity of biomolecular response, both with and without AuNPs. Our study reveals that the electrostatic interactions between carboxyl-modified AuNPs and positively charged histidine induce a localized field enhancement effect at the interface between the biomolecule and the terahertz metamaterial. This interaction results in a threefold improvement in response sensitivity relative to histidine without AuNPs, leading to a significant increase in both the MD and ME factors. In contrast, for glucose, the response sensitivity enhancement is less pronounced, due to the absence of electrostatic interactions between the electrostatically neutral glucose molecules and AuNPs. We further investigated the relationship between the resonance coupling of the metamaterial at different frequency positions and the characteristic frequencies of the biomolecules. The experimental results indicate that the response sensitivity of terahertz metamaterial reaches a high level at the EIT frequency, which is close to the characteristic frequency of the biomolecule. As the concentration of the biomolecule solution increases, the MD and ME factors for histidine at the EIT1 peak, which is near its characteristic frequency, consistently exceed those for glucose. This allows for intuitive and highly efficient label-free detection and distinguish of these two biomolecules. Additionally, by constructing this two-EIT metamaterial with a 1×2 pixel array, we demonstrated the ability for multiparameter biomolecular imaging, facilitating the visualization of the concentration and spatial distribution of various biomolecules. The findings not only offer novel perspectives for the design of functionalized terahertz biosensors but also present effective strategies for achieving high-sensitivity biomolecular detection and differentiation, opening new avenues for high-throughput biomolecular analysis and diagnostic imaging in complex biological systems.

Results and discussion

Figure 1a illustrates the experimental workflow for studying biomolecular solutions based on functionalized AuNPs. These nanoparticles are functionalized with thiolated polyethylene glycol carboxylic acid (SH-PEG-COOH), where the thiol groups (–SH) form stable Au–S bonds with gold atoms on the nanoparticle surface. The polyethylene glycol (PEG) chains provide a balance between hydrophobicity and hydrophilicity, enhancing the stability and biocompatibility of the particles in aqueous solutions. Under slightly acidic pH conditions ($pH \leq 6$), the carboxyl groups (–COOH) partially dissociate to form negatively charged carboxylate ions ($–COO^-$), imparting negative charges to the nanoparticle surface (the functionalization process is detailed in the

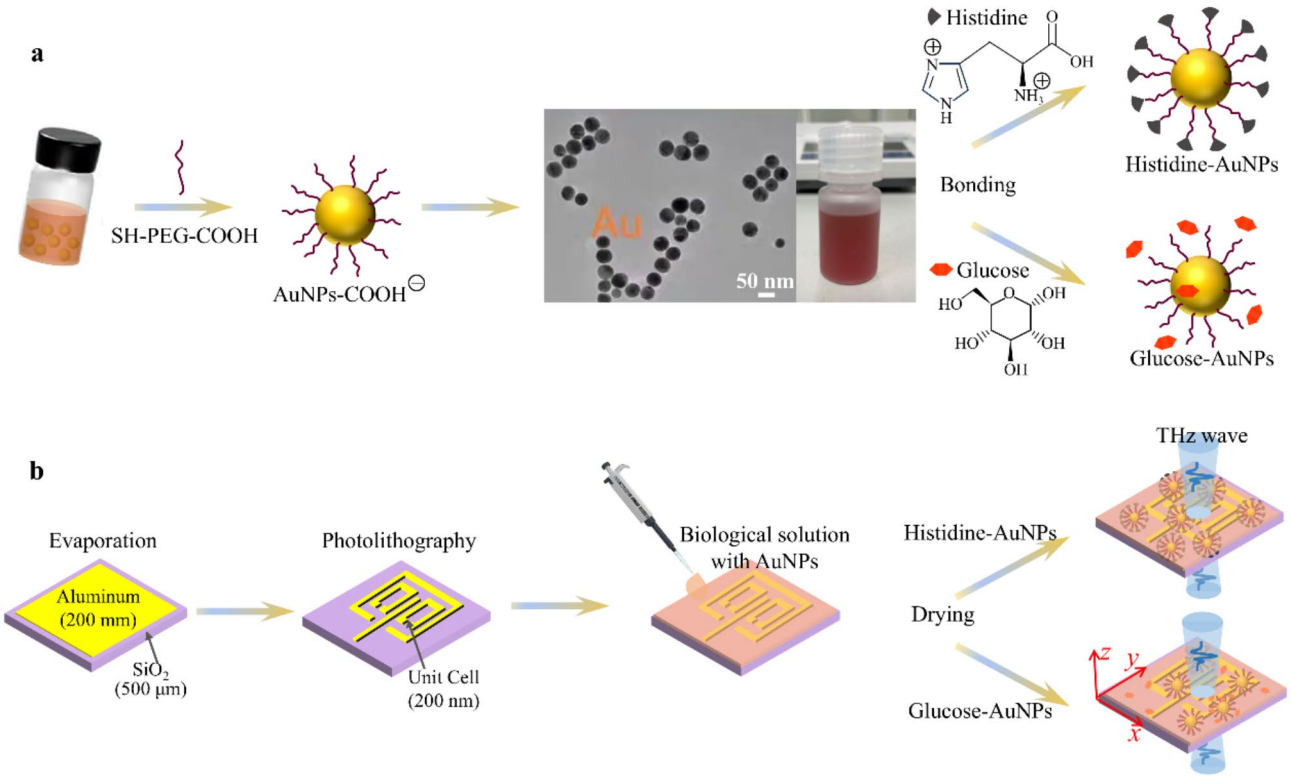

Fig. 1. Working principle and preparation of the two-EIT terahertz metamaterial based on biomolecules with AuNPs. (**a**) Schematic diagram for the workflow of the developed functionalized AuNPs bonded with the respective histidine and glucose, along with the SEM image of the AuNPs. (**b**) Preparation of the metamaterial periodic arrays, followed by the dripping and drying of biomolecule solutions with AuNPs onto the metamaterial surface. The incidence direction of the THz wave is along the indicated *z*-axis. AuNPs and biomolecules are not drawn to scale, and the number of biomolecules per AuNP and metamaterial unit cell is believed to be much more than depicted.

Methods). Due to the interaction between biomolecules and AuNPs with the diameter of approximately 50 nm enhances the terahertz response signal[47], the prepared carboxyl-modified AuNPs colloid (pH ≤ 6) has an average diameter of approximately 50 nm, as characterized by scanning electron microscope (SEM). Histidine, an amino acid containing an imidazole side chain, becomes positively charged under acidic and neutral pH conditions due to the protonation of its imidazole group and amino group ($-NH_3^+$). Consequently, histidine predominantly exists in a cationic form in these environments[40]. When introduced to the negatively charged carboxyl-modified AuNPs, electrostatic attraction leads to the adsorption of histidine onto the nanoparticle surface. In contrast, glucose is a monosaccharide lacking charged functional groups in its molecular structure. As a result, glucose solutions are electrically neutral and do not undergo electrostatic interactions with the negatively charged AuNPs. Figure 1b shows the proposed two-EIT terahertz metamaterial sensors. The periodic unit of the metamaterial is made up of one cut wire and three split-ring resonators (CThSRRs). The size of the entire metamaterial array is 8.91 mm × 8.91 mm, The metamaterial structures are fabricated via photolithography on a 500 μm thick SiO_2. The metamaterial structures are made of 200 nm-thick Aluminum. The optical microscope images of the fabricated metamaterials are shown in Supplementary Fig. S1. The geometrical parameters of the periodic unit are illustrated in Fig. 2a and Supplementary Fig. S2. Then the histidine and glucose solution with different concentrations both with and without functionalized AuNPs were dripped on the surface of the two-EIT metamaterial and dried to form films. We measured the response sensitivity to biomolecules by monitoring the relative changes in the resonance-coupling peaks of transmission spectra between the sample and bare two-EIT metamaterial for all samples. A bare SiO_2 substrate without metamaterials is used as the reference.

Figure 2a shows the schematic representation of the designed terahertz metamaterial, adopted from our previous work in Ref.[24], and has been optimized in terms of structural dimensions based on that study. By uniformly scaling the entire unit cell, the transmission spectra the metamaterial at various size scaling factors were first characterized using simulations. when the size was 0.9 times that in Ref. 24, we defined the scaling factor as k = 0.9. When the size matched that in Ref. 24 (P = 90 μm), k = 1. When the size was increased to 1.1 times that in Ref. 24 (P = 99 μm), k = 1.1. As shown in Fig. 2b, the transmission spectra have an obviously redshift, as the k increased from 0.9 to 1.1. The first transmission peak shifted from 1.02 THz to 0.83 THz, while the first resonance dip moved from 0.90 THz to 0.74 THz. The characteristic frequency of histidine molecules, measured to be around 0.8 THz (Supplementary Fig. S3a), which is exactly between the first transmission peak and the first resonance dip at k = 1.1. Therefore, the metamaterial sensors we will discuss next are all based

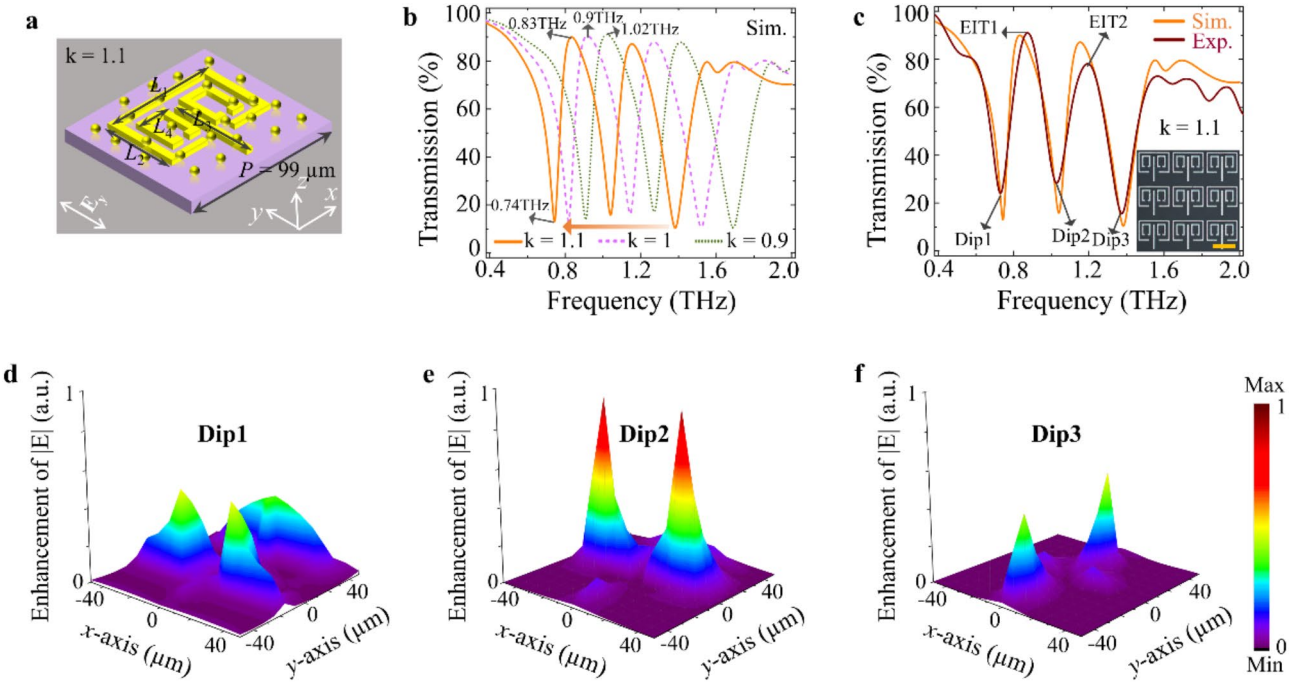

Fig. 2. Simulation and experimental results of the two-EIT metamaterial under y-orientation polarized incident radiation. (**a**) Periodic unit. (**b**) Simulated transmission spectra under different scaling factors (k = 0.9, 1, 1.1). (**c**) Experimental (Exp.) and simulated (Sim.) transmission spectra at k = 1.1. The inset is the optical microscope images of the fabricated metamaterial. Scale bar: 60 μm. (**d**–**f**) 3D E-field enhancement maps at the frequencies of Dip1, Dip2 and Dip3. Geometrical parameters at k = 1.1 are $P = 99$ μm, $L_1 = 92.4$ μm, $L_2 = 61.6$ μm, $L_3 = 69.3$ μm, $L_4 = 26.4$ μm.

on the two-EIT metamaterial configuration with k = 1.1. The strong resonance at approximately 0.8 THz in histidine powder originates from low-frequency vibrational modes due to the coupling between the imidazole ring and the hydrogen-bond network in its solid-state structure[46,48]. This mode produces a distinct absorption peak in the terahertz spectrum, serving as a characteristic fingerprint of histidine in this frequency range[48]. In contrast, the vibrational modes generated by the coupling between the pyranose ring and the intermolecular hydrogen bond network in the molecular structure of glucose are mainly reside in the relatively high terahertz region[6]. The numerically and experimentally studied transmission spectra (normalized) of the metamaterial in the absence of biomolecules and AuNPs are plotted in Fig. 2c. Three resonance dips appear at approximately 0.74 THz, 1.04 THz, and 1.38 THz, designated as Dip1, Dip2, and Dip3. Two transmission peaks at about 0.83 THz and 1.15 THz are denoted as EIT1 and EIT2, respectively. The operational frequency range of the metamaterial extends from 0.74 THz to 1.38 THz. To elucidate the formation mechanism of these resonance coupling peaks, the 3D E-field enhancement maps across the unit cell at the three resonance frequencies were simulated, under y-polarized incident wave. As depicted in Fig. 2d, the enhanced electric field at Dip1 primarily arises from a ring-dipole resonance in the Big SRR. At Dip2, shown in Fig. 2e, the significant enhanced field results from the LC resonance generated at the openings of the two small SRRs. At Dip3, shown in Fig. 2f, a dipole resonance is induced by the CW element, leading to electric field enhancement at both ends. The coupling among these three resonance modes gives rise to the two observed transmission peaks. Due to the strong local field enhancements, the resonance-coupling of these three modes can be highly sensitive to environmental perturbations, analogous to localized surface plasmons-based bio (chemical) sensors[49,50]. The design of this two-EIT metamaterial with three resonant bands and two transparency peaks offers distinct advantages. Firstly, the introduction of three resonant modes is crucial for achieving two EIT windows. The generation of two EIT windows requires coupling among at least three resonant modes, while the coupling of two resonant modes or a single resonant mode is insufficient to create two transparency windows[24]. Furthermore, a single resonant mode cannot evaluate the response sensitivity of biomolecules at both transmission peak and resonance frequency band, and lacks the capability for comparison at multiple frequency points. The two EIT windows in this design enable the metamaterial to simultaneously evaluate the biomolecular response sensitivity at the EIT peaks corresponding to different frequencies. The EIT1 transparency peak (0.83 THz) is near the characteristic frequency of histidine (0.8 THz), while the EIT2 transparency peak is far away from this frequency, allowing for comparative analysis to determine whether the EIT1 transparency peak close to the biomolecular characteristic frequency exhibits higher response sensitivity. Similarly, the first resonant band (0.74 THz) is near the histidine characteristic frequency, while the other two bands are positioned away from this frequency. This also enables the metamaterial to analyze the effects of different resonant bands at various frequencies on biomolecular detection. Additionally, this two-EIT metamaterial with three-resonance avoids the complex active or passive tuning of resonant and

coupling frequencies, thus simplifying its biomolecular detection process. To verify the biosensing performance of the two-EIT metamaterial and to investigate the enhancement in response sensitivity provided by the AuNPs, we investigated the response properties of histidine and glucose molecules (with and without AuNPs) at three resonance dips and two transmission peaks. Each measurement was repeated six times ($n = 6$), and the error bars in the experimental data represent the standard error of the mean.

The histidine and glucose solution, both with and without AuNPs were added on the surface of the metamaterials, respectively. Due to the strong absorption of terahertz waves by water molecules in the biological solution, it is difficult to achieve the transmission-based concentration analysis of the biological solution[34,51,52]. Thus, we crystallized the biological solution at a temperature of 60℃ to form a dried film (the heat drying process is detailed in the Methods). The effect of biomolecular solution volume on metamaterial performance was evaluated using histidine (10 mg/mL) as a representative sample. Applying 30 µL often resulted in incomplete spreading across the entire metamaterial array due to surface tension, contact angle effects, and insufficient volume (the area inside the orange dashed box in Supplementary Fig. S4). Despite subsequent heating promoting liquid flow and crystallization, noticeable gaps remained at the center and localized regions, leading to a discontinuous and non-uniform film (Supplementary Fig. S4a). These conditions hindered the acquisition of comparable measurements. Increasing the volume to 40 µL, the biological solution formed a relatively continuous crystalline film after heating and drying. However, differences in the flap-like structure were observed in some areas, resulting in a slightly insufficient thickness uniformity compared with 50 µL (Supplementary Fig. S4b). Nevertheless, 40 µL was sufficient to produce measurable differences (Supplementary Fig. S5) and was identified as the minimum feasible sample volume. When the volume is increased to 50 µL, the solution spread rapidly and uniformly across the metamaterial surface. After heating and drying, faint radial patterns appeared on the film surface, but overall uniformity and compactness were maintained (Supplementary Fig. S4c). Additionally, repeated terahertz measurements exhibited reduced error (Supplementary Fig. S5), ensuring stable signal intensity and high reproducibility. Thus, 50 µL was selected as the standard droplet volume for subsequent experiments. We selected a histidine concentration range of 1 ~ 40 mg/mL for the following reasons. First, previous studies report that histidine is typically used at 1 ~ 30 mg/mL in antioxidant and anti-inflammatory tests[53], and at 5 ~ 50 mg/mL in the detection of histidine specific adsorbed immunoglobulin[54]. Second, our experiments revealed that histidine concentrations below 1 mg/mL yield insufficient film coverage, while those above 40 mg/mL significantly increased viscosity, causing uneven crystallization and compromising subsequent measurements. Finally, this concentration range allows for the evaluation of the stability and linear response of the metamaterial device at both low and high biomolecule concentrations. This ensures our results are applicable to biological assays that require a wide concentration range, such as drug screening, cell culture, and in vitro analysis. Therefore, selecting 1 to 40 mg/mL accommodates a variety of biomedical scenarios while maintaining experimental feasibility and robust detection sensitivity. This also highlights the importance and relevance of this chosen concentration range for the metamaterial biosensor research and the biological studies. For comparison, glucose was prepared using the same concentration range to elucidate differences in terahertz response between histidine and glucose.

The terahertz spectrum for histidine and glucose at 5 mg/mL on bare SiO_2 substrate did not show distinguishable features compared to the spectrum for a bare SiO_2 wafer (Supplementary Fig. S3b). Histidine powder pressed into a pellet exhibits a significant absorption peak at 0.8 THz, corresponding to its intrinsic characteristic frequency (Supplementary Fig. S3a). However, in Supplementary Fig. S3b, the dried histidine solution film does not show an absorption peak at this frequency. The reason is that as the drying process alters the molecular arrangement, resulting in an extremely small absorption cross section of the molecule at the relevant terahertz frequency regime[6]. Therefore, the results demonstrate that the disappearance of the intrinsic absorption peak of histidine is attributed to the change in physical state (from solid powder to dried crystalline film), rather than the resonant coupling effect of the metamaterial or AuNPs. As shown in Supplementary Fig. S6a, the terahertz spectrum of histidine with AuNPs on bare SiO_2 substrate show no distinguishable features, confirming that the presence of AuNPs in the histidine solution did not introduce new resonance or coupling peaks. In the absence of biomolecules, the terahertz transmission spectra of the two-EIT metamaterial and the two-EIT metamaterial based AuNPs show no significant differences (Supplementary Fig. S6b), indicating that AuNPs do not exhibit resonant or coupling responses to the incident terahertz wave[34]. Thus, the addition of AuNPs alone does not induce insertion loss. However, the terahertz spectroscopy changes of two-EIT metamaterials remarkably in the presence of biomolecules with AuNPs, indicating that the presence of AuNPs affects the interaction between the metamaterial and biomolecules.

The influence of AuNPs diameter and concentration in the biological solution on the sensitivity of the metamaterial for biomolecular detection was examined separately. The biomolecules integrated with AuNPs can be regarded as a film of the isotropic medium according to effective medium theory. In this case, increasing the AuNPs diameter is equivalent to increasing the thickness of the film sample. The simulation results show that with the increase of sample film thickness, the transmittance peak of EIT1 shows a decreasing trend, as shown in Supplementary Fig. S7a. It can be inferred that biomolecules modified with 50 nm AuNPs exhibit a greater reduction in the transmission peak than those with smaller AuNPs. Previous experiments have further confirmed that increasing the AuNP diameter from 20 nm to 50 nm enhances response sensitivity[47]. Based on this explanation, larger AuNPs (e.g., 100 nm) should theoretically result in a persistent reduction in transmittance peaks. However, experiments show that increasing the AuNP diameter from 50 nm to 100 nm in a histidine solution (10 mg/mL) reduces the decreasing amplitude of the transmission peak value, that is, the peak transmission value of EIT1 increased, as shown in Supplementary Fig. S7b. This anomaly is attributed to the tendency of larger AuNPs to form too large aggregates, reducing their dispersion on the metamaterial surface, particularly in high electromagnetic field regions such as aperture gaps and metallic edges. This aggregation weakens resonance coupling, thereby diminishing the transmission peak variation. Supplementary Fig. S7c

shows the change in the EIT1 transmission peak ($\delta T_{\max}$) for varying concentration of AuNPs from 0 to 50 μg/mL. $\delta T_{\max}$ is given by:

$$\delta T_{\max} = T_{C_{0\text{-AuNPs}}\max} - T_{C_{c\text{-AuNPs}}\max} \quad (1)$$

where $C_{0\text{-AuNPs}}$ refers to the AuNPs concentration of 0 μg/mL in the 10 mg/mL of histidine solution. $C_{c\text{-AuNPs}}$ refers to the AuNPs corresponding concentration in the 10 mg/mL of histidine solution. $T_{C_{0\text{-AuNPs}}\max}$ is the measured transmission peak of the two-EIT metamaterials for histidine (10 mg/mL) without AuNPs. $T_{C_{c\text{-AuNPs}}\max}$ refers to the measured transmission peak of the two-EIT metamaterials for histidine (10 mg/mL) with the corresponding AuNPs concentration. Experimental results reveal that $\delta T_{\max}$ initially increases with AuNPs concentration, reaching its peak at 25 μg/mL. Beyond this threshold, further concentration increments lead to a slight decline in $\delta T_{\max}$. This phenomenon can be attributed to the following: under low concentration conditions (< 25 μg/mL), as AuNP concentration increases, more nanoparticles can interact with biomolecules, promoting the enrichment of biomolecules in the local region of the metamaterial surface. This enrichment enhances biomolecule-metamaterial coupling, intensifies the local electromagnetic field, significantly alters the transmittance, and improves the response sensitivity of the device. When the AuNPs concentration is further increased (> 25 μg/mL), the electrostatic repulsion between AuNPs becomes insufficient to counteract interparticle attraction, leading to heterogeneous aggregation. This aggregation reduces the specific surface area of AuNPs and weakens the resonance coupling effect of the device. Moreover, as AuNPs concentration increases, its influence on the surrounding medium approaches saturation[55]. Consequently, excessively high AuNPs concentrations result in a weaker reduction of the EIT1 transmission peak, thereby reducing the response sensitivity of metamaterial to biomolecules. The above experimental results indicate that the AuNPs with 50 nm diameter and 25 μg/mL in the biological solution, yield the greatest reduction in the transmission peak of the two-EIT metamaterial. Therefore, all subsequent analyses of two-EIT metamaterials coupled with AuNPs integrated with biomolecules are based on these optimized AuNPs parameters.

Figure 3 and Supplementary Fig. S8 show the experimental biosensing results of the two-EIT metamaterial in different concentrations of histidine and glucose, both with and without AuNPs. Firstly, in the presence of AuNPs, the frequency shifts observed in the Dip1 to Dip3 for both histidine and glucose remain largely consistent with those recorded in the absence of AuNPs (Fig. 3a,d). This phenomenon suggests that the addition of AuNPs has a minimal effect on the dielectric properties of histidine and glucose. Secondly, in biomolecular solutions with and without AuNPs, the variation in the transmission peak demonstrates a significantly sharper contrast compared

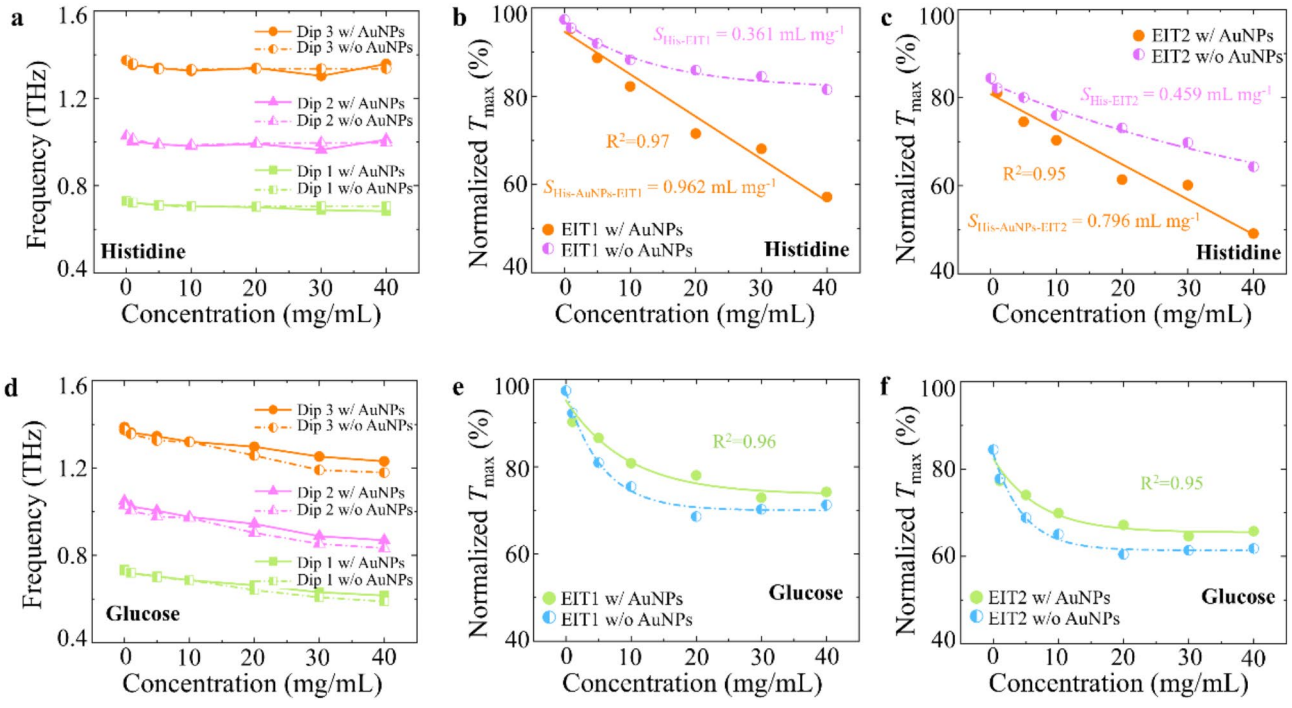

Fig. 3. Experimental biosensing results of linearly polarized illumination on the two-EIT metamaterial. The frequencies of three transmission dips (Dip1, Dip2, Dip3) for different concentrations of (**a**) histidine and (**d**) glucose, both with (w/) and without (w/o) AuNPs. Normalized transmission peaks (T_{max}) of EIT1 windows with their fitting results for different concentrations of (**b**) histidine and (**e**) glucose, both with and without AuNPs. The correlation coefficients of these fitting lines are $R^2_{EIT1-histidine}$ = 0.97, $R^2_{EIT1-glucose}$ = 0.96. Normalized transmission peaks (T_{max}) of EIT2 windows with their fitting results for different concentrations of (**c**) histidine and (**f**) glucose, both with and without AuNPs. The correlation coefficients of these fitting lines are $R^2_{EIT2-histidine}$ = 0.95, $R^2_{EIT2-glucose}$ = 0.95.

to the frequency shift of the resonance band (Fig. 3). For glucose, being electrically neutral, its molecules do not exhibit significant electrostatic interactions with AuNPs. Thus, the addition of AuNPs fails to substantially modify the dielectric constant of the glucose, resulting in a consistent frequency shift in the metamaterial irrespective of AuNP presence. For histidine, the weak dielectric response and polarization saturation effect contribute to its minimal change in dielectric constant. The polar groups of histidine, such as amino and carboxylic groups, approach polarization saturation at low concentrations, so the effect of concentration changes on the resonant dips frequencies of metamaterials is extremely limited. The electrostatic interaction between histidine and AuNPs mainly enhances the local electromagnetic coupling between the molecule and the metamaterial. However, it has minimal impact on the dielectric constant, leading to small frequency shifts in the resonance dip. This further limits the applicability of the resonance dip as a sensitivity indicator, making it unreliable as a standard for sensitivity measurement. In contrast, the electrostatic interaction between histidine and AuNPs enhances the local electromagnetic coupling between the biomolecule and the metamaterial, increasing optical absorption and scattering losses, which leads to a significant decrease in the EIT transmission peak. Therefore, the magnitude of the decrease in the transmission peak more accurately reflects the sensitivity of the metamaterial to histidine molecules than the resonant dip frequency shift, which makes it a superior indicator of response sensitivity. In addition, in the presence of AuNPs, the transmission peak reduction observed in the EIT1 and EIT2 for both histidine exhibits more pronounced changes compared to those without AuNPs. Therefore, the transmission peak change is selected as the index of the characteristic response of biomolecules with and without AuNPs. The response sensitivity S is used to characterize the reduction in the EIT peak of the two-EIT metamaterial, which is given by:

$$S=\frac{\Delta T_{\max}}{\Delta C}=\frac{T_{0\max}-T_{c\max}}{C_c\text{-}C_0} \tag{2}$$

where $\Delta T_{\max}=T_{0\max}-T_{c\max}$ is the change in the transmission peak. $T_{0\,\max}$ and $T_{c\,\max}$ refer to the measured transmission peak of the two-EIT metamaterials and the corresponding biomolecule solution, respectively. $\Delta C=C_c\text{-}C_0$ is the change in biomolecule concentration. C_0 refers to the biomolecule solution concentration of 0 mg/mL. C_c refers to the corresponding concentration of biomolecule solution. As shown in Fig. 3b, the EIT1 transmission peak of the two-EIT metamaterials at 0.83 THz showed a good linear relationship with the concentration of histidine containing AuNPs. The corresponding response sensitivity is $S_{\mathrm{AuNPs-EIT1}}$ = 0.962 mL mg^{-1}, which is around 3 times higher than the response sensitivity of EIT1 transmission peak for histidine concentration without AuNPs (S_{EIT1} = 0.361 mL mg^{-1}). As shown in Fig. 3c, the response sensitivity of the EIT2 transmission peak for histidine concentration with AuNPs is $S_{\mathrm{AuNPs-EIT2}}$ = 0.796 mL mg^{-1}, which is around 2 times higher than the detection sensitivity of EIT2 transmission peak for histidine concentration without AuNPs (S_{EIT1} = 0.459 mL mg^{-1}). The enhanced response sensitivity of the two-EIT metamaterial to histidine with AuNPs is attributed to the stable binding between the -COOH-modified AuNPs and positively charged histidine molecules formed by electrostatic interaction. This stable binding effectively enriches histidine molecules in the localized regions of the metamaterial surface, thereby strengthening the molecule–metamaterial coupling and enhancing the local electromagnetic field effects. This enhanced field effect significantly increases the optical absorption and scattering losses of the metamaterial, leading to a more pronounced decrease in the EIT transmission peak. In the presence of AuNPs, the reduction in the EIT1 peak is greater than that of the EIT2 peak, indicating that the response sensitivity of EIT1 is higher than that of EIT2. Furthermore, the characteristic frequency of histidine (0.80 THz) is located near the frequency of EIT1 (0.83 THz). Therefore, the results indicate that the transparency window at EIT1, which is close to the characteristic frequency of histidine, exhibits high response sensitivity to histidine modified with AuNPs.

The EIT transmission peak of the two-EIT metamaterials for glucose with and without AuNPs are plotted in terms of the concentration levels with exponential decay fittings, as shown in Fig. 3e,f. With increasing glucose concentration, the reduction in the EIT transmission peak is less pronounced in the presence of AuNPs than in their absence. This phenomenon can be attributed to three factors. First, this behavior arises from the uncharged nature of glucose molecules, which precludes effective electrostatic interactions with the negatively charged AuNPs. Consequently, the AuNPs fail to significantly enhance the coupling between glucose molecules and the metamaterial, resulting in minimal amplification of the local field effect. Second, the introduction of AuNPs establishes additional scattering pathways, facilitating energy dissipation through alternative mechanisms, which partially offsets the reduction in the EIT transmission peak. Third, the presence of AuNPs induces heterogeneity in the local field enhancement, thereby reducing the overall sensitivity of the metamaterial to dielectric responses.

The weakening of the transmission peak reduction caused by adding biomolecule samples without AuNPs can be explained by the following interpretations. Due to the dielectric loss of the sensing target, the energy of the incident THz wave is reduced[34]. At low concentrations, fewer biomolecules per unit area result in little influence on the incident wave energy and a larger decrease in transmission peak amplitude. At high concentrations, there are more biomolecules per unit area, causing reduction of the incident wave energy and reducing the decrease in transmission peak amplitude[24]. For glucose samples with AuNPs, the attenuation in the transmission peak decrease remains apparent, primarily due to the inability of glucose molecules to form electrostatic interactions with AuNPs. This precludes a significant enhancement in the coupling between glucose molecules and the metamaterial. In contrast, histidine samples with AuNPs demonstrate a linear decrease in the transmission peak amplitude. This phenomenon arises from the ability of positively charged histidine molecules to form stable complexes with negatively charged AuNPs via electrostatic interactions. Such interactions sustain the persistence and stability of the local field enhancement effect, resulting in a linear relationship between the EIT peak amplitude decrease and concentration.

As shown in Fig. 4, an in-depth analysis was conducted to compare the differences in the maximum values of normalized experimental transmittance for the metamaterial under conditions with and without AuNPs, using a biomolecule concentration of 10 mg/mL as a representative example. The results indicate that the introduction of AuNPs allows the EIT1 transmission peak value at a low histidine concentration of 10 mg/mL to reach a level comparable to that observed at a higher concentration of 30 mg/mL without AuNPs. Similarly, the EIT2 transmission peak at 10 mg/mL histidine with AuNPs matches the level of 20 mg/mL without AuNPs. This finding provides further evidence that introducing AuNPs significantly enhances the response sensitivity of the metamaterial, particularly for EIT1 peaks that are proximate to the characteristic frequency of histidine, resulting in an approximately threefold improvement. In contrast, the introduction of AuNPs leads to a slight reduction in the EIT1 transmission peak at a low glucose concentration of 10 mg/mL, compared to the peak observed at the same concentration of glucose without AuNPs.

While these changes in the EIT peak reflect the differences in concentration and response sensitivity of histidine and glucose with AuNPs, it is difficult to distinguish between them. Therefore, we further investigated the MD and ME factor of the biomolecular samples on the two-EIT metamaterial. MD is defined as $MD = (|T_{0\max} - T_{c\max}|)/T_{0\max}$. The ME factor is represented by $ME = MD_A/MD_0$, where MD_0 and MD_A are the transmission-dependent modulation depth without and with AuNPs, respectively. Due to the enhanced response sensitivity of histidine at EIT1 as demonstrated by the aforementioned study, we will mainly focus on measuring and calculating the MD and ME for histidine and glucose, both with and without AuNPs at EIT1 of the two-EIT metamaterial, as shown in Fig. 5. Although it increases with the biological concentration, the MD of histidine with and without AuNPs exhibits a huge difference at the same concentration, as illustrated in Fig. 5a. This observation suggests that the electrostatic interaction between AuNPs and the negatively charged histidine enhances the local electromagnetic field coupling at the metamaterial interface, thereby inducing a higher carrier density. Considering that both the resonance coupling strength of the metamaterial and the electrostatic binding effect between AuNPs and histidine significantly contribute to the modulation behavior, the increased histidine concentration further strengthens the electrostatic interaction, resulting in a more pronounced modulation enhancement effect in the metamaterial. For instance, at a concentration of 40 mg/mL, the MD at EIT1 of the metamaterial for histidine with and without AuNPs is 42.2% and 16.3%, respectively. In contrast, at the same concentration, the MD of glucose with and without AuNPs exhibits minimal variation. Specifically, at 40 mg/mL, the MD at EIT1 of the metamaterial for glucose with and without AuNPs is 21.3% and 26.8%, respectively (Fig. 5b). This observation suggests that the electrostatically neutral glucose molecules prevent the formation of electrostatic interactions with AuNPs, leading to a relatively weak synergistic effect and, consequently, a lack of significant enhancement in the electromagnetic response of glucose within the metamaterial. At this concentration (40 mg/mL), the ME factors for histidine and glucose are 2.6 and 0.8, respectively, demonstrating that the ME for histidine is markedly higher than that for glucose.

Additionally, we compared the MD at EIT1 transmission peak ($|MD_{\text{His-AuNPs}}|$ and $|MD_{\text{glu-AuNPs}}|$ for histidine and glucose, with AuNPs, respectively) on the two-EIT metamaterial and calculated the modulation depth difference ΔMD at different concentrations (Fig. 5c), which is defined as

$$\Delta MD = |MD_{\text{His-AuNPs}}| - |MD_{\text{Glu-AuNPs}}| \tag{3}$$

It can be seen the ΔMD are positive, which means that the ΔMD of histidine with AuNPs is always larger than the glucose with AuNPs at different concentrations, then, it is easy to distinguish the biomolecular species between histidine and glucose intuitively from the values of the modulation depth difference ΔMD. As observed in the ME spectra (Fig. 5a, b), a clear distinction in the ME is evident between histidine and glucose at the same concentration. As the concentration increases, the ME for histidine exceeds 1, indicating a marked enhancement, whereas the ME for glucose shows a gradual increase but consistently remains below 1. The difference between

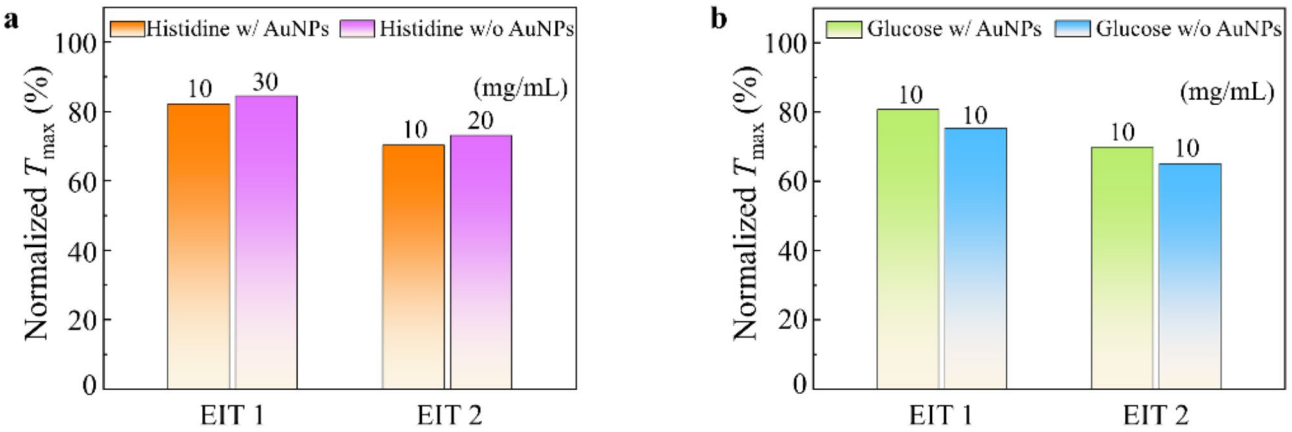

Fig. 4. Normalized transmission peaks (T_{max}) of two EIT windows (EIT1 and EIT2) for a 10 mg/mL concentration of (**a**) histidine and (**b**) glucose, both with AuNPs, corresponding to the concentration levels at which the transmission peaks are comparable to those observed without AuNPs.

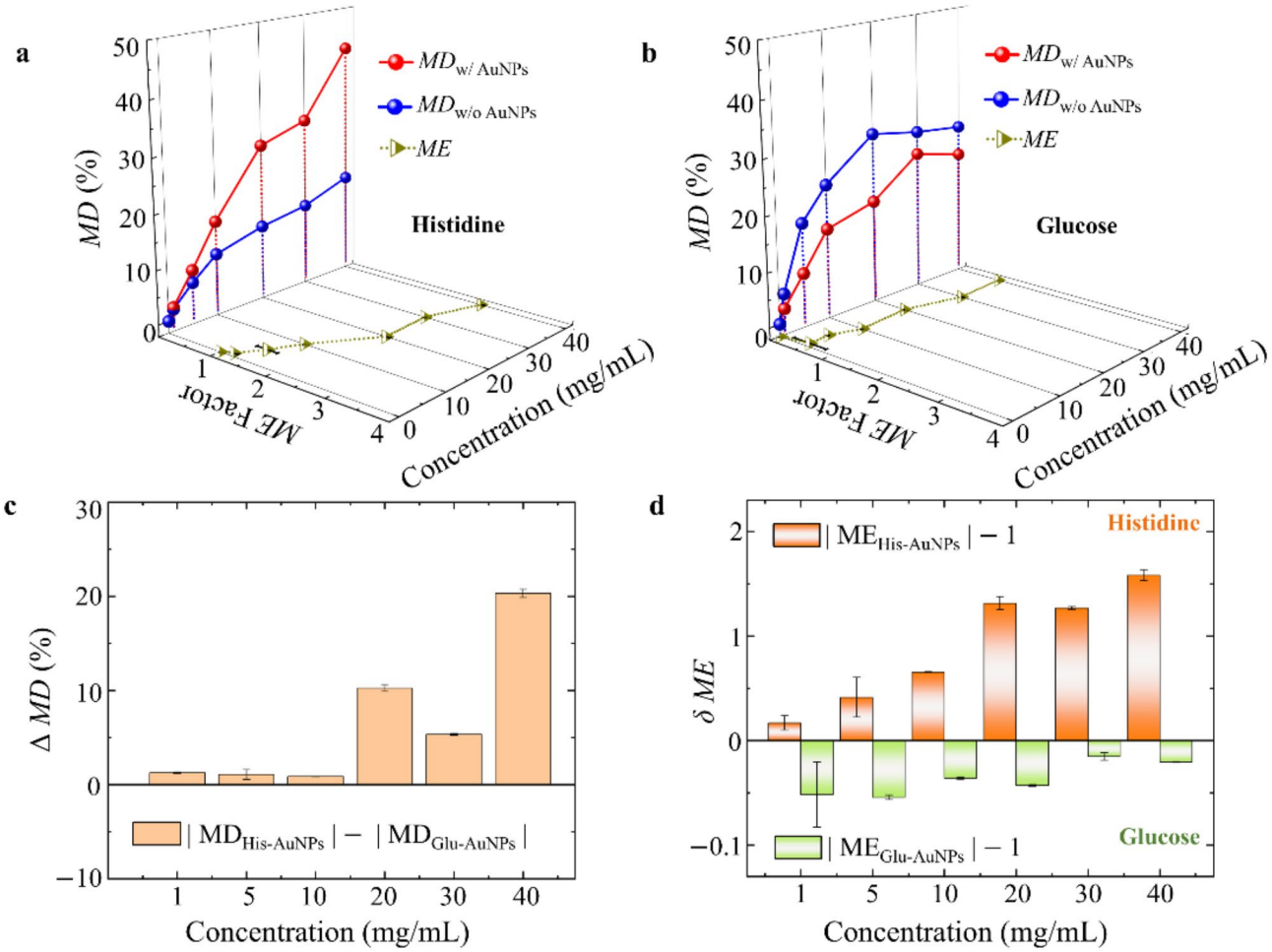

Fig. 5. Transmission-dependent modulation depth at EIT1 of (**a**) histidine and (**b**) glucose, both with and without AuNPs, and the corresponding ME factor as a function of biomolecule concentrations. (**c**) Δ*MD* and (**d**) *δME* values for histidine with AuNPs and glucose with AuNPs with different biomolecule concentrations.

the ME and 1 at different concentrations for the same biomolecule is defined as $\delta ME = |ME| - 1$. It can be seen that as the concentration increases, *δME* for histidine remains invariably positive, while the glucose counterpart is consistently negative (Fig. 5d). These positive and negative values of *δME* further realized the qualitative and intuitive distinction of histidine and glucose molecules, highlighting the recognition capability of the two-EIT metamaterial and AuNPs toward these two types of biomolecules. Although the proposed strategy currently lacks the ability to explicitly distinguish different biomolecules in mixed biological solutions or mixed dried films through the spectra responses of multi-EIT metamaterials, the integration of AuNPs holds significant promise for achieving high-sensitivity detection of diverse biomolecules.

The two-EIT metamaterial devices based on multi-resonance coupling bands exhibit advantages in biological response sensitivity and modulation depth, making them promising for the construction of this device in terahertz biological imaging applications. Here, a terahertz imaging system is employed to convert the modulation depth information derived from the two-EIT metamaterial into image signals for biomolecular detection, facilitating the simultaneous visualization of both the concentration and spatial distribution of different biomolecules. We present a 1×2 pixel array formed by two biomolecules based on a single metastructure, allowing spatial control of terahertz transmission at individual array positions, as shown in Fig. 6a, with the terahertz electric field along the y-axis. It is mentioned above that the transmission spectrum will undergo a red shift with increasing biomolecular concentration so that the transmission variation at a fixed frequency cannot reflect the degree of resonant-coupling modulation. Considering the different sensitivities of EIT peaks at various frequency positions to biomolecular concentration and type, we display their imaging patterns of the selected histidine and glucose in the EIT1 and EIT2 regions (As shown in Fig. 6b). Figure 6b displays the images using the false color to represent the transmission-dependent modulation depth with and without AuNPs. The color gradient, ranging from purple (low modulation depth) to red (high modulation depth), indicates the extent of interaction between glucose and histidine with the metamaterial under these varying conditions. The specific mapping of the modulation depth in this color-coded representation allows for an intuitive understanding of the concentration and the effectiveness of AuNPs in enhancing terahertz responses. As the biomolecular concentration increases, distinct multicolor imaging emerges. Notably, upon the introduction of AuNPs to histidine, color differentiation

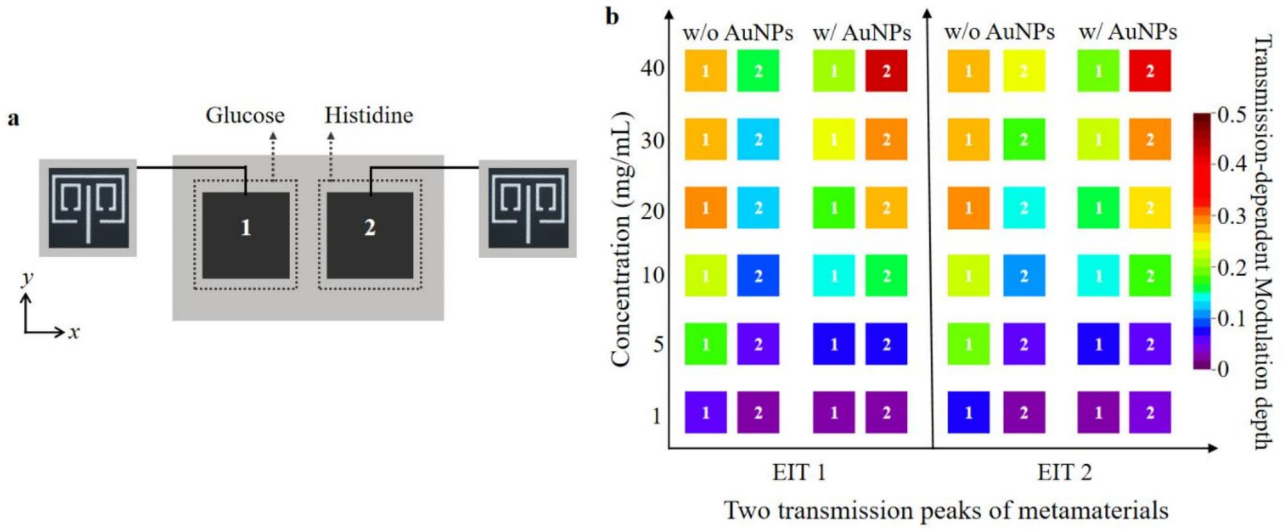

Fig. 6. Biomolecular detection imaging display of two-EIT metamaterials. (**a**) Schematic construction of the two-EIT pixel arrays with terahertz E-field along the y-axis. (**b**) Imaging display using spectrum color pattern to represent transmission-dependent modulation depth of EIT1 and EIT2 at different biomolecule concentrations with and without AuNPs.

becomes more evident, and the colored image more rapidly shifts towards red, reflecting a significant enhancement in modulation depth corresponding to the EIT1 and EIT2 modes. This underscores the role of AuNPs in amplifying localized field effects, thereby substantially improving the overall response sensitivity. This phenomenon is particularly pronounced in EIT1, as the frequency of EIT1 closely aligns with the characteristic frequency of histidine, leading to enhanced response sensitivity, clearly demonstrated by the transition in the transmission peak change ΔT_{max} across different concentrations (Supplementary Fig. S9). Here we have demonstrated the imaging of two-EIT metamaterial based on two biomolecules with a 1×2 array to emphasize the multiparameter imaging function by using transmission-dependent modulation depth. By incorporating additional biomolecules into an expanded array, it is anticipated that complex imaging patterns can be realized, drawing on transmission-dependent modulation depth, frequency response, and variations in biomolecular concentrations under conditions with and without AuNPs. This multiparameter imaging approach, rich in diverse information, holds great promise for advancing terahertz bio-imaging systems.

Conclusions

In summary, we have developed a sensitive terahertz biosensor based on two-EIT metamaterials coupled with AuNPs integrated with biomolecules. The high sensitivity of this sensor is attributed to the electrostatic interactions between carboxyl-modified AuNPs and positively charged histidine. This interaction generates local field enhancements at the biomolecule-metamaterial interface, significantly improving the response sensitivity for histidine that are weakly sensitive to dielectric properties varying with concentration. Specifically, the transmission peak of metamaterial corresponding to histidine exhibits significantly increased MD and ME factors, thus providing a robust mechanism for the efficient detection of low-concentration biomolecules. Conversely, the absence of electrostatic interactions between electrically neutral glucose molecules and AuNPs results in a less pronounced sensitivity enhancement for glucose detection. The experimental results reveal that with increasing biological solution concentrations, the MD and ME values for histidine at the EIT1 peak, which is proximal to its characteristic frequency, consistently exceed those of glucose. This enables intuitive and highly efficient label-free detection and differentiation of these two biomolecules. Furthermore, the integration of a two-EIT metamaterial with a 1×2 pixel array demonstrates the capability for multiparameter biomolecular imaging, enabling the visualization of biomolecular concentration and spatial distribution. These findings not only underscore the potential of AuNP-enhanced terahertz metamaterials for biomolecular detection but also pave the way for the development of advanced high-sensitivity biosensing platforms, offering new opportunities for high-throughput biomolecular analysis and diagnostic imaging.

Methods

Reagents

Histidine powder and glucose powder were purchased from Aladdin, while AuNPs and thiolated polyethylene glycol carboxylic acid (SH-PEG-COOH) were procured from Macklin. Deionized water was used to prepare solutions of varying concentrations of histidine and glucose, both with and without functionalized AuNPs.

Functionalization process of AuNPs

The functionalization of AuNPs was achieved by mixing AuNP solution with HS-PEG-COOH, followed by gentle stirring for over 10 h. The functionalized AuNP-COOH solution was stored in the dark at 4 °C to maintain stability for subsequent applications. The AuNP-COOH solution was centrifuged twice (30 min each) to eliminate any unbound HS-PEG-COOH. The purified AuNP-COOH was resuspended in 4-morpholineethanesulfonic acid (MES) buffer (pH = 5.5).

Incorporation of biomolecules and AuNPs

Adding histidine and glucose, respectively. Positively charged histidine was add and gently stirred to promote electrostatic interactions with the functionalized AuNPs. Glucose was introduced to the functionalized AuNPs, and the mixture was gently stirred to ensure uniform dispersion.

Preparation of biomolecule pellets

The histidine and glucose powders were formed into pellets with polyethylene (PE) at a mixing ratio of 1:1, respectively. The thickness of pellets is about 1 mm, the diameter is about 13 mm, and the mass is about 200 mg (the inset in Supplementary Fig. S3a).

Fabrication of two-EIT terahertz metamaterial sensors

A mask bearing the two-EIT metamaterial array was first adhered onto the SiO_2 substrate, followed by electron-beam evaporation of a 200 nm aluminum film. A 500 nm-thick photoresist layer was then spin-coated onto the substrate, and the pattern of metamaterial structure was exposed using laser direct write lithography. The exposed sample was wet etched to complete the preparation of the two-EIT metamaterial. Then 50 μL of the histidine and glucose solution with different concentrations both with and without functionalized AuNPs (25 μg/mL) were dripped on the surface of the two-EIT metamaterial and dried at 60℃for 15 min to form a dried film. The heat drying process was as follows: The metamaterial sample was placed on the heating stage, ensuring good thermal contact. The stage was preheated to 30 °C and maintained for 2 min to achieve uniform metamaterial surface heating and reduce temperature gradients. 50 μL of biomolecular solution was added to the upper surface of the preheated metamaterial to ensure that the droplets spread in a gently heated environment. This reduces the problem of uneven appearance due to uneven evaporation rates. The sample remained at 30 °C for an additional 2 min to ensure a stable distribution of the liquid film before further heating. Subsequently, the temperature was gradually increased at a rate of 5 °C/min over 6 min to reach 60 °C, preventing abrupt evaporation rate changes, minimizing local concentration fluctuations, and ensuring the formation of a uniform thin film. Finally, the sample was held at 60 °C for 15 min to complete the drying process, yielding a homogeneous thin film. Reproducibility experiments were conducted under identical heating conditions, and terahertz spectra were repeatedly measured (as shown in Supplementary Fig. S10). The slight deviations, indicated by the error bars, confirm the stability of the dried biofilm morphology.

Simulation of the two-EIT terahertz metamaterial

Simulations were conducted using Computer Simulation Technology Microwave Studio (version 2019, CST, Darmstadt, Germany). The SiO_2 substrate is described by a dielectric constant of 3.58 with loss tangent delta of 0.01. The linearly polarized incident wave is perpendicular to the metamaterial surface.

Experimental measurement of terahertz transmission of metamaterials sensors

All measurements are characterized by a transmission-type terahertz time-domain spectroscopy system (THz-TDS), as shown in Supplementary Fig. S11. The femtosecond laser oscillator used for the broadband terahertz beam has a repetition rate of 80 MHz and is purchased from Coherent. The spectral bandwidth is set to 70 nm. The pulsed laser beam with 800 nm center wavelength is focused onto a photoconductive switch. This system has a bandwidth of 0.1 THz to 2.0 THz by Fourier transform. The beam waist diameter of the terahertz beam (3 mm) was much smaller than the periodic array on the sample, thus ensuring measurement validity[56].

Data availability

The datasets used and/or analyzed during the current study are available from the corresponding author on reasonable request.

Received: 1 January 2025; Accepted: 10 March 2025
Published online: 12 March 2025

References

1. Jiang, L. et al. Terahertz optoacoustic detection of aqueous salt solutions. *iScience* **25**(7), 104668 (2022).
2. Wei, L. et al. Application of Terahertz spectroscopy in biomolecule detection. *Front. Med.* **2**(4), 127–133 (2018).
3. Koch, M., Mittleman, D. M., Ornik, J. & Castro-Camus, E. Terahertz time-domain spectroscopy. *Nat. Rev. Methods Primers* **3**(1), 48 (2023).
4. Walther, M., Fischer, B., Schall, M., Helm, H. & Jepsen, P. U. Far-infrared vibrational spectra of all-trans, 9-cis and 13-cis retinal measured by Thz time-domain spectroscopy. *Chem. Phys. Lett.* **332**(3), 389–395 (2000).
5. Bessou, M. et al. Three-dimensional terahertz computed tomography of human bones. *Appl. Opt.* **51**(28), 6738–6744 (2012).
6. Lee, D. K. et al. Highly sensitive and selective sugar detection by Terahertz nano-antennas. *Sci. Rep.* **5**(1), 15459 (2015).
7. Janke, C., Först, M., Nagel, M., Kurz, H. & Bartels, A. Asynchronous optical sampling for high-speed characterization of integrated resonant terahertz sensors. *Opt. Lett.* **30**(11), 1405–1407 (2005).
8. Ruggiero, M. T., Sibik, J., Orlando, R., Zeitler, J. A. & Korter, T. M. Measuring the elasticity of poly-l-proline helices with terahertz spectroscopy. *Angew Chem. Int. Ed.* **55**(24), 6877–6881 (2016).

9. Yang, K., Yang, X., Lamy de la Chapelle, M. & Fu, W. Thz spectroscopy for a rapid and label-free cell viability assay in a microfluidic chip based on an optical clearing agent. *Anal. Chem.* **91**(1), 785–791 (2019).
10. Zhang, M. et al. Flexible specific determination of glucose in solution, blood serum, and sweat using a Terahertz hydrogel-functionalized metamaterial. *Adv. Mater. Technol.* **8**(21), 2300775 (2023).
11. Shen, S. et al. Recent advances in the development of materials for Terahertz metamaterial sensing. *Adv. Opt. Mater.* **10**(1), 2101008 (2022).
12. Li, J. et al. A review: Active tunable Terahertz metamaterials. *Adv. Photonics Res.* **5**(7), 2300351 (2024).
13. Li, Q., Liu, S., Zhang, X., Wang, S. & Chen, T. Electromagnetically induced transparency in terahertz metasurface composed of meanderline and u-shaped resonators. *Opt. Express.* **28**(6), 8792–8801 (2020).
14. Choi, M. et al. A Terahertz metamaterial with unnaturally high refractive index. *Nature* **470** (7334), 369–373 (2011).
15. Simovski, C. R., Belov, P. A., Atrashchenko, A. V. & Kivshar, Y. S. Wire metamaterials: physics and applications. *Adv. Mater.* **24**(31), 4229–4248 (2012).
16. Zhang, M. et al. Chiral biosensing using Terahertz twisted chiral metamaterial. *Opt. Express* **30**(9), 14651–14660 (2022).
17. Xiao, B., Tong, S., Fyffe, A. & Shi, Z. Tunable electromagnetically induced transparency based on graphene metamaterials. *Opt. Express* **28**(3), 4048–4057 (2020).
18. Wu, W. et al. Optical rotation and electromagnetically induced transparency in a chiral metamaterial with c4 symmetry. *Opt. Express* **28**(20), 29496–29512 (2020).
19. Yue, Y. et al. Analogue of electromagnetically induced transparency in a metal-dielectric bilayer terahertz metamaterial. *Opt. Express* **29** (2021).
20. Yan, X. et al. The Terahertz electromagnetically induced transparency-like metamaterials for sensitive biosensors in the detection of cancer cells. *Biosens. Bioelectron.* **126**, 485–492 (2019).
21. Zhou, J. et al. Molecule-specific Terahertz biosensors based on an aptamer hydrogel-functionalized metamaterial for sensitive assays in aqueous environments. *ACS Sens.* **6**(5), 1884–1890 (2021).
22. Tao, H. et al. Metamaterials on paper as a sensing platform. *Adv. Mater.* **23**(28), 3197–3201 (2011).
23. Cui, Z. et al. Coupling-based multiple bound states in the continuum and grating-assisted permittivity retrieval in the terahertz metasurface. *ACS Appl. Mater. Interfaces.* **16** (6), 7631–7639 (2024).
24. Zhang, M. et al. Exploring the application of multi-resonant bands Terahertz metamaterials in the field of carbohydrate films sensing. *Biosensors* **13**(6), (2023).
25. Wang, P. et al. Plasmonic metamaterials for nanochemistry and sensing. *Acc. Chem. Res.* **52**(11), 3018–3028 (2019).
26. Wei, X., Ren, C., Liu, B., Peng, Y. & Zhuang, S. The theory, technology, and application of terahertz metamaterial biosensors: A review. *Fundam. Res.* (2024).
27. Khodaie, A. & Heidarzadeh, H. Evaluation of severe acute respiratory syndrome coronavirus 2 (sars-cov-2) using a high figure-of-merit plasmonic multimode refractive index optical sensor. *Sci. Rep.* **14** (1), 25499 (2024).
28. Zhang, W. et al. Terahertz metamaterials for biosensing applications: A review. *Biosensors* **14**(1), (2024).
29. Matyushov, D. V. On the theory of dielectric spectroscopy of protein solutions. *J. Phys. : Condens. Matter.* **24**(32), 325105 (2012).
30. Tomić, S. et al. Dielectric relaxation of DNA aqueous solutions. *Phys. Rev. E* **75**(2), 021905 (2007).
31. Bakewell., D. J., Irigaray, N. V. & Holmes, A. Dielectrophoresis of biomolecules. *JSM Nanotechnol Nanomed.* **1**(1), 1003 (2013).
32. Qiu, G. et al. Dual-functional plasmonic photothermal biosensors for highly accurate severe acute respiratory syndrome coronavirus 2 detection. *ACS Nano* **14**(5), 5268–5277 (2020).
33. Chen, Z. et al. Rapid and sensitive detection of anti-sars-cov-2 Igg, using lanthanide-doped nanoparticles-based lateral flow immunoassay. *Anal. Chem.* **92**(10), 7226–7231 (2020).
34. Xu, W. et al. Gold nanoparticle-based Terahertz metamaterial sensors: Mechanisms and applications. *ACS Photonics* **3**(12), 2308–2314 (2016).
35. Kumalasari, M. R., Alfanaar, R. & Andreani, A. S. Gold nanoparticles (aunps): A versatile material for biosensor application. *Talanta Open* **9**, 100327 (2024).
36. Guliy, O. I. & Dykman, L. A. Gold nanoparticle–based lateral-flow immunochromatographic biosensing assays for the diagnosis of infections. *Biosens. Bioelectron. : X* **17**, 100457 (2024).
37. Ngernpimai, S. et al. Enhanced stability of gold nanoparticles with thioalkylated carboxyl-terminated ligands for applications in biosensing. *ACS Appl. Nano Mater.* **7**(11), 13124–13133 (2024).
38. Bian, T. et al. Electrostatic co-assembly of nanoparticles with oppositely charged small molecules into static and dynamic superstructures. *Nat. Chem.* **13**(10), 940–949 (2021).
39. Yanik, A. A. et al. An optofluidic nanoplasmonic biosensor for direct detection of live viruses from biological media. *Nano Lett.* **10**(12), 4962–4969 (2010).
40. Calinsky, R. & Levy, Y. Histidine in proteins: Ph-dependent interplay between π–π, cation–π, and ch–π interactions. *J. Chem. Theory Comput.* **20**(15), 6930–6945 (2024).
41. Chen, Y. et al. Histidine as a key modulator of molecular self-assembly: Peptide-based supramolecular materials inspired by biological systems. *Mater. Today* **60**, 106–127 (2022).
42. Chen, S. et al. Single nanoparticle identification coupled with auto-identify algorithm for rapid and accurate detection of l-histidine. *Anal. Chim. Acta.* **1187**, 339162 (2021).
43. Tang, S. et al. A near-infrared fluorescence capillary imprinted sensor for chiral recognition and sensitive detection of l-histidine. *Anal. Chim. Acta* **1206**, 339794 (2022).
44. Schneider, F. Histidine in enzyme active centers. *Angew Chem. Int. Ed. Engl.* **17**(8), 583–592 (1978).
45. Yadav, S. et al. Crystal growth and optical, nonlinear optical, thermal and Terahertz time domain spectra of l-histidine single crystal: A potential Terahertz material. *ACS Appl. Opt. Mater.* **1**(11), 1791–1800 (2023).
46. Bian, Y., Zhu, Z., Zhang, X., Zeng, R. & Yang, B. Terahertz spectroscopy for quantitatively elucidating the crystal transformation of chiral histidine enantiomers to racemic compounds. *Food Chem.* **406**, 135043 (2023).
47. Yang, K. et al. A terahertz metamaterial biosensor for sensitive detection of micrornas based on gold-nanoparticles and strand displacement amplification. *Biosens. Bioelectron.* **175**, 112874 (2021).
48. True, A. B., Schroeck, K., French, T. A. & Schmuttenmaer, C. A. Terahertz spectroscopy of histidine enantiomers and polymorphs. *J. Infrared Millim. Terahertz Waves* **32**(5), 691–698 (2011).
49. Haes, A. J. & Van Duyne, R. P. A unified view of propagating and localized surface plasmon resonance biosensors. *Anal. Bioanal Chem.* **379**(7–8), 920–930 (2004).
50. Mayer, K. M. & Hafner, J. H. Localized surface plasmon resonance sensors. *Chem. Rev.* **111**(6), 3828–3857 (2011).
51. Xu, W. et al. Terahertz biosensing with a graphene-metamaterial heterostructure platform. *Carbon* **141**, 247–252 (2019).
52. Ahmadivand, A. et al. Functionalized terahertz plasmonic metasensors: Femtomolar-level detection of sars-cov-2 spike proteins. *Biosens. Bioelectron.* **177**, 112971 (2021).
53. Wade, A. M. & Tucker, H. N. Antioxidant characteristics of l-histidine 11the work described in this manuscript was partially sponsored and funded by cytos pharmaceuticals, llc. *J. Nutr. Biochem.* **9**(6), 308–315 (1998).
54. Du, Z., Zhang, S., Zhou, C., Liu, M. & Li, G. L-histidine functionalized multi-walled carbon nanotubes for on-line affinity separation and purification of immunoglobulin g in serum. *Talanta* **99**, 40–49 (2012).
55. Liang, L. et al. Graphene and gold nanoparticles integrated Terahertz metasurface for improved sensor sensitivity. *Phys. E* **156**, 115842 (2024).

56. Zhang, S. et al. Nonvolatile reconfigurable Terahertz wave modulator. *PhotoniX* **3**(1), 7 (2022).

Acknowledgements
This work was supported by the Natural Science Youth Foundation of Shandong Province (No. ZR2024QF278), and the Qingdao Municipal Fund for Postdoctoral Foundation (No. QDBSH20240102172).

Author contributions
M.Z. conceived the idea and initiated the design with input from Z.T. proposed the terahertz biosensing with gold nanoparticle coupled metamaterials concepts and designed the study. M. Z. fabricated the metamaterial sensor, performed metamaterial characterization, performed the transmissive-THz experiment measurement, and completed the biomolecules detection. S. Z. fabricated the two-EIT metamaterial. M. Z. and S. W. analyzed simulation results. M. Z. and L. J. purchased and fabricated the biomaterial. M. L., Y.Z., H.Z. and Z.T. provided suggestions on designing experiments and analyzing the results. M.Z., Y.Z, H.Z. and Z.T. wrote and revised the manuscript. Z. T. and H.Z. supervised the project. All authors of this paper agree to publish.

Declarations

Competing interests
The authors declare no competing interests.

Additional information
Supplementary Information The online version contains supplementary material available at https://doi.org/10.1038/s41598-025-93850-4.

Correspondence and requests for materials should be addressed to H.Z. or Z.T.

Reprints and permissions information is available at www.nature.com/reprints.

Publisher's note Springer Nature remains neutral with regard to jurisdictional claims in published maps and institutional affiliations.